Spatial arrangements and types of dislocations in interfacial networks obtained by Si(001) wafer bonding at low twist angle : a TEM characterization

Loïc Patout, Claude Alfonso, Marion Descoins, Frank Fournel, Dominique Mangelinck, Nathalie Mangelinck-Noël

Spatial arrangements and types of dislocations in interfacial networks obtained by Si(001) wafer bonding at low twist angle : a TEM characterization

L. Patout[1], C. Alfonso[1], M. Descoins[1], F. Fournel[2], D. Mangelinck[1] & N. Mangelinck-Noël[1]

loic.patout@im2np.fr

[1]Aix-Marseille Univ., Université de Toulon, CNRS, IM2NP, Marseille, France

[2]CEA-LETI, Université Grenoble-Alpes, Grenoble, France

Keywords

Interface; Dislocation network; Nanostructuring; Wafer bonding; Deformation mechanisms

Abstract

Two interfacial dislocation networks were obtained in a Si-Si material system by wafer bonding process for low twist angles around 0.2°. For one sample, one of the two initial wafers was rotated with an additional angle of 90° before the bonding. TEM analyses of samples prepared for planar and transverse views show different characteristics in terms of spatial arrangement and dislocation types. Long climbing segments slightly deviated from the [100] axis and short segments **a/2<101>** are arranged in the dislocation network obtained with an additional rotation and at the lowest twist angle ($\Psi = 0.18°$) from a <110> axis. Long screw segments **a/2<110>** and short partial Shockley segments are arranged in the dislocation network obtained without any additional rotation at the highest twist angle ($\Psi = 0.27°$) from a <110> axis. In both cases, the long and short segments form elongated hexagonal patterns, which are accurately ordered in one set paving the <100> directions or randomly ordered in two perpendicular sets paving the <110> directions, respectively. The results are discussed taking into account the arangement of the surface miscut steps in the initial wafers before the bonding.

1. Introduction

The field of crystal defect engineering continually opens new perspectives in the creation of new materials, processes and applications. Dislocations fundamentally influence many physical and mechanical properties of crystalline solids. Mechanical properties, such as work hardening, are related to the generation and interaction of a large number of dislocations, while electrical properties are affected by only a few of these defects. In the latter case, individual dislocations can have adverse effects on the electrical parameters of semiconductor devices, especially for nanoscale dimensions. These are also major defects of the silicon ingots produced for photovoltaic solar cells with respect to their efficiency even for industrial production of large ingots **[1]**. In addition, dislocations can promote the growth of different nanostructures that can be deleterious for device processing **[2]**.

Before the 1990s, the main method applied for the generation of dislocations was plastic deformation. However, this method has the disadvantage of introducing a large number of different defects and defect reactions, which sometimes makes it difficult to control the generated dislocations and therefore to interpret the experimental data. Wafer bonding (WB) is an alternative to generate defined geometries of dislocation networks. This process is widely used in MEMS devices to create SOI structures as well as cavities or channels to connect parts in sensors and actuators for which it was originally developed **[3]**. The technique is based on the fact that two mirror-polished solid surfaces of Si that are sufficiently flat and clean stick spontaneously together when brought into contact **[4].** They are first attracted to each other by Van der Waals forces after a slight pressure which quickly establishes a high density of H-H bonds between the two surfaces. Then, an annealing at high temperature makes it possible to achieve a sufficient mechanical strength thanks to the creation of covalent Si-Si bonds **[5].**

The interface properties of the bonded Si bicrystals mainly depend on the surface state of the wafer (hydrophilic, hydrophobic, oxidized) due to the environment (air, vacuum or

deionized water) before assembly. With an oxygen-free interface, which is the case in this study, the electrical properties are related to the concentration and distribution of dangling bonds at the interface. With a buried SiO_2 layer, they are also determined by the homogeneity of the bonding and the contamination level in the oxidation interfaces **[6].** The period of the strain field generated by the network of buried interfacial dislocations and the characteristics of ohmic junctions between two bonded wafers strongly depend on the relative crystal misorientation **[7, 8]**.

As a potential application, the biperiodic strain field generated by the wafer bonding, alternating compressed and dilated areas at the surface, can be used to drive epitaxial nanostructure growth, providing a simple, inexpensive and low-temperature process **[9]**. Deposition of both lattice-matched (unstrained areas) and lattice-mismatched (compressed or dilated areas) nanoscale materials rotated on similar materials have already been exploited. This method has allowed to provide substrates for subsequent growth of heteroepitaxial layers without defects **[10]**. In the 2000s, encouraging results in the perspective of ordering quantum dots for applications to optical emitters were obtained **[11]**. This method has also been successfully used to design new substrates and thin films of various materials to answer to the demands of the industry **[12, 13]**. The resulting interfaces of the bonded Si bicrystals can be viewed as giant grain boundary (GB) models, whose dislocation structures are crucial to understand for the improvement of nanostructured devices in the microelectronics technology.

In this study, we characterize two dislocation networks in Si-Si interfaces prepared by wafer bonding using misorientation angles close to 0°. Such configurations are not discussed extensively in the literature concerning the role of angular mismatches, in particular those prepared by adding a 90°-rotation of a wafer in the pair before the bonding.

2. Experiment

A wafer bonding process generates two types of misorientation between the two crystals consisting of a twist angle Ψ around the normal ***n*** with respect to ***u*** parallel to the bonding interface, and a tilt angle θ around a direction ***u(⊥n) (Fig. 1a)***. Initial cutting errors (miscuts) of (001) silicon wafers are generally not specified with an accuracy better than 0.5°, therefore, bonded wafer processes cannot completely avoid uncontrolled tilt misorientations. Moreover, both are not independent, since any change of the twist angle influences the tilt angle. Depending on the respective angle values, wafer bonding generates sets of dislocations which differ in their type, distance and length. From simple geometric considerations, the distance D_d between dislocations of same type is given by the Frank's rule:

$$D_d = \frac{b}{2\sin(\frac{\Phi}{2})} \quad \text{(Eq. 1)},$$

where b and Φ are the magnitude of the Burgers vector and the misorientation angle, respectively **[14]**.

2.1.Material

Two networks of dislocation segments (DN1 and DN2) were obtained by wafer bonding carried out at low twist angle close to 0°. Given the lack of control over wafer miscut mentioned above, an additional uncertainty of ± 1° is also expected on the tilt angle. The effective angles of twist and tilt were calculated after the wafer bonding from the distances measured between each type of dislocations compensating for each misorientation.

The samples were prepared by the following procedure ***(Fig. 1b)***. Two monocrystalline silicon wafers with a diameter of 200 mm and a thickness of 725 µm are used. The first one is a SOI (Silicon On Insulator) substrate bought from SOITEC company. It is composed of a substrate with a thermal oxide layer of 200 nm and a top silicon thin film of 100 nm. The top

silicon film is a <001> with a resistivity around 10 Ω.cm. The second substrate is a bulk P-doped silicon <001> wafer with a resistivity around 10 Ω.cm as well.

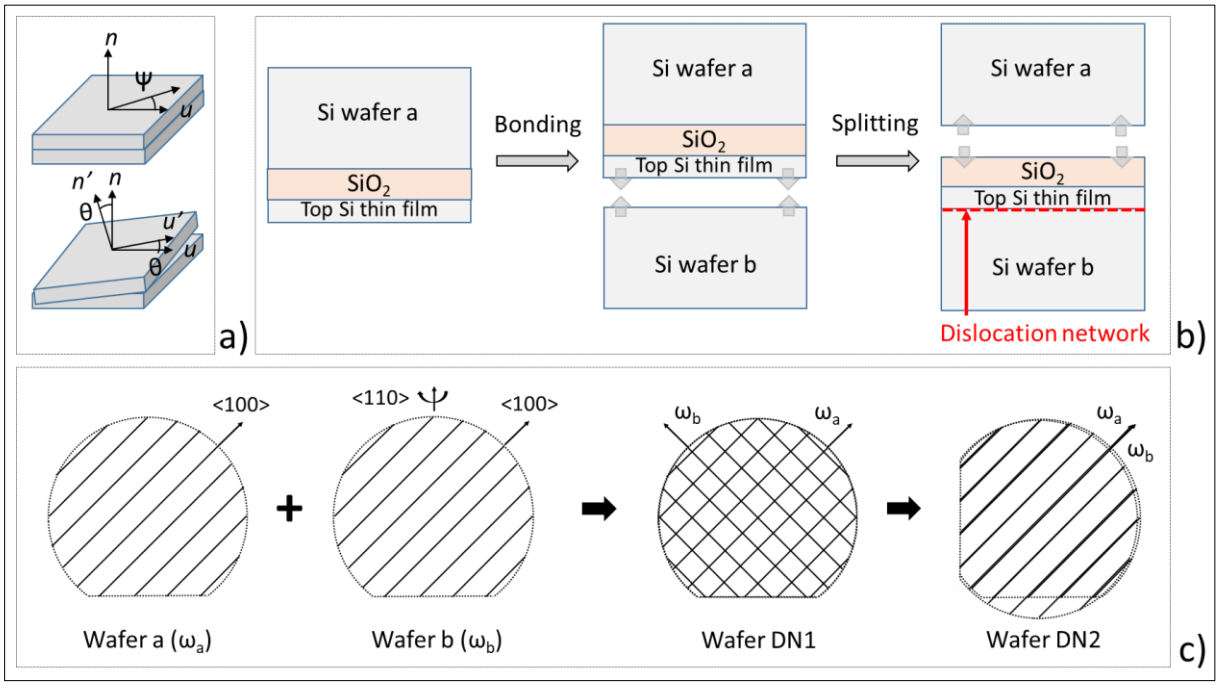

Figure 1: Wafer bonding process. (a) The misorientation is composed of two rotations : a twist angle Ψ around the normal ***n*** to the bonding interface, and a tilt angle θ with respect to ***u(⊥n)*** due to the miscut between the wafers. (b) The main steps of the manufacturing process. (c) Twist angles applied between the wafers a and b giving DN1 and DN2. DN2 has an additional twist of 90° compared to DN1.

Both substrates are cleaned using a standard mixture of sulfur peroxide and ammonium peroxide in order to remove any contamination. Then, they are treated by hydrofluoric acid with a concentration of 1% during 1 minute. This treatment removes the native oxide and passivates the chemical bonds of the silicon surfaces with hydrogen. After rinsing of the surfaces, made hydrophobic, with deionized water for 30 s, the substrates are brought into contact in a clean room atmosphere. Before bonding, the twist angle between both wafers was achieved in two different ways. For DN1, one of the two similar wafers was flipped 180° around an axis <110> perpendicular to the notch. As a result, the interface contains the two sets of surface miscut steps from each initial wafer along two perpendicular directions <100>. For DN2, the flipped wafer was additionally rotated by 90° in the bonding plane giving a single set of surface miscut

steps along one direction <100> ***(Fig. 1c)***. The direct bonding is initiated with a pin force of less than 2 N. Then, the structure is annealed at 1200°C during 2 hours under nitrogen with 1% of O_2. The backside of the SOI substrate is mechanically polished using a grinding tool allowing to remove a thickness of 625 µm. The last 100 µm are removed with a conventional hydrofluoric acid/nitric acid mixture stopping on the buried oxide layer used as a practical etch stop layer. The oxide layer is maintained in order to protect the silicon thin film during the TEM sample preparation.

2.2.Preparation of the TEM samples

Lamellae were prepared by mechanical polishing of the bonded wafers in two orientations [001] and [110], in order to observe the DNs by transmission electron microscopy (TEM) in planar and cross sections, respectively ***(Fig. 2)***. For the cross-section lamella, two bonded wafers were stuck together by the oxide faces, then the polishing was carried out perpendicular to the 2D network ***(Fig. 2a)***. For the plane view lamella, only the non-oxidized face of a bonded wafer was polished ***(Fig. 2b)***. The lamellae were ground down to a thickness of 1 µm using progressively finer grit SiC abrasive paper down to 0.1µm in roughness. Then, they were thinned down to about 250 nm using a Precision Ion Polishing System (PIPS-Gatan) operating with Ar using progressively reduced energies, from 5 kV to 2 kV, and incidence angles relative to the face lamella from 8° to 2°, respectively. The size of a TEM lamellae represents a small portion of the whole samples. Several planar and transverse lamellae were prepared in each case (DN1 and DN2), in very distant positions. The arrangements of the dislocation networks observed in each lamella were all similar for DN1, as well as for DN2.

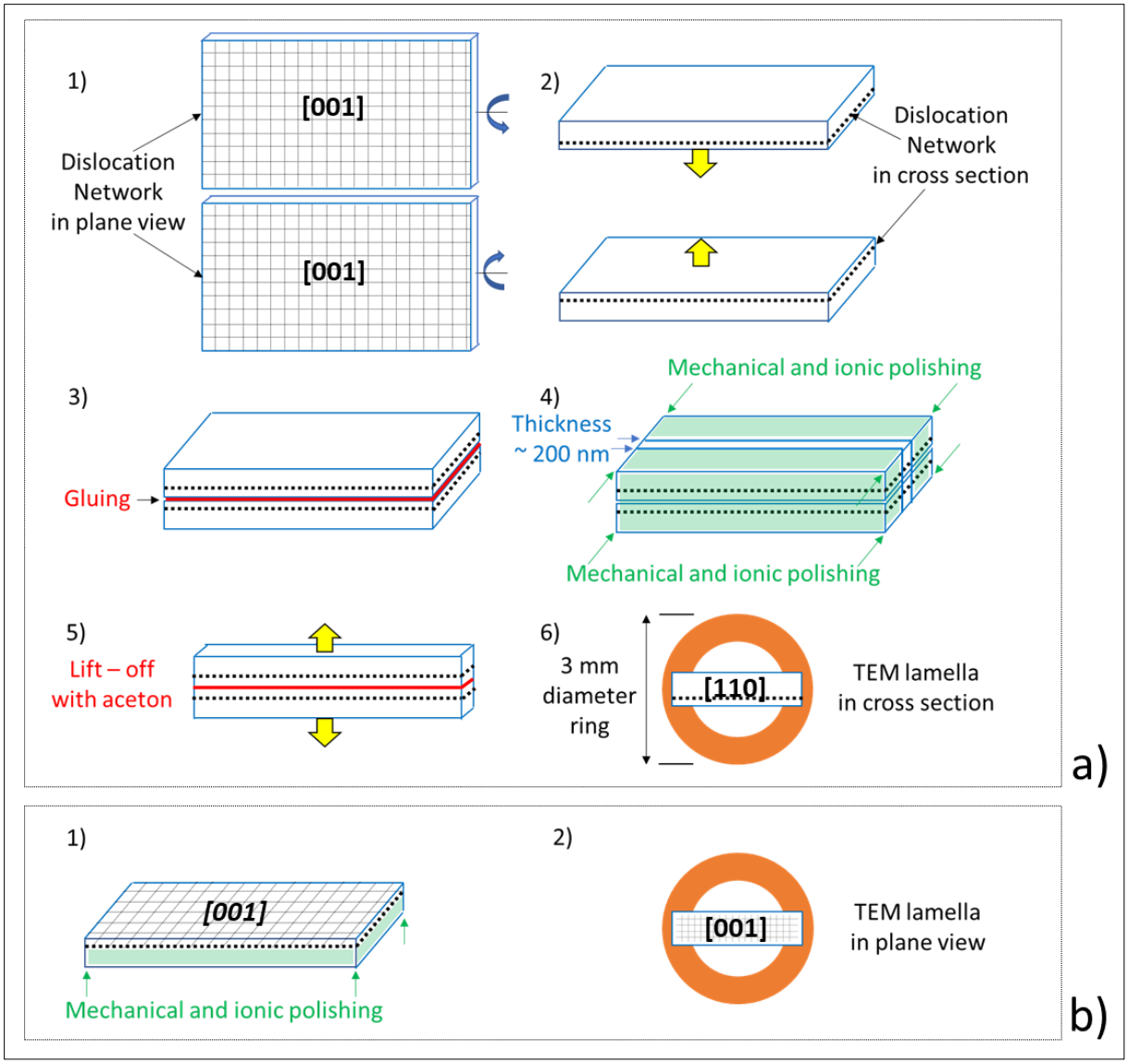

Figure 2: Preparation of the TEM lamellae in [110] cross-section (a) and [001] plane-view (b).

2.3. TEM characterization

The high-resolution electron microscopy (HREM) analyses were carried out with a Field Emission Gun Thermofisher Titan TEM microscope equipped with a spherical aberration (Cs) correction system. The Cs value is between 0 and -0.05 mm allowing a point-to-point resolution of around 1 Å **[15, 16].** The bright (BF) and dark field (DF) analyses in conventional and scanning (STEM) mode were carried out with a LaB_6 Thermofisher Tecnai microscope. The experimental TEM images were processed with Digital Micrograph software **[17]**. The crystal models of dislocation networks were drawn with CrystalMaker **[18]**.

3. Results

3.1. DN1

A BF-TEM image of the plane-view lamella in [001] zone axis shows a fairly periodic network ***(Fig. 3a)*** composed of dislocation segments aligned along two perpendicular directions, forming square patterns. The segments were also observed by diffraction contrast using the two-beam dark field (DF) imaging technique to determine the direction and the type of the dislocations. The Burgers vectors can be determined by the invisibility criteria $\boldsymbol{g}.\boldsymbol{B} = 0$ ($\boldsymbol{g}$ = diffraction vector, $\boldsymbol{B}$ = Burgers vector), and by tilting the same area of analysis to obtain a set of images using different $\boldsymbol{g}$ vectors. DF images were performed using perpendicular diffraction wave vectors, namely $\boldsymbol{g}(\bar{2}\bar{2}0)$ and $\boldsymbol{g}(\bar{2}\bar{2}0)$. The results show that the perpendicular segments constituting the network of squares are both aligned along <110> directions ***(Fig. 3b)***. The contrast is off for wave vectors perpendicular to the line directions, but on for parallel vectors, which is consistent with the screw nature of **a/2<110>** dislocations classically encountered in face-centered cubic bulk materials **[19]**.

However, DN1 differs from the perfect 2D model of lines by the characteristic presence of three-fold segments similar to those also observed by Boussaid et al., consisting of a long **a/2<110>** screw dislocation segment (yellow) connected to two short segments (red) **[20]**. The bright contrast of the short segments (red arrows) whatever the vector, $\boldsymbol{g}(\bar{2}\bar{2}0)$ and $\boldsymbol{g}(\bar{2}\bar{2}0)$, is consistent with the presence of screw and edge components for these dislocations **[21]**. Rousseau et al., indicated from HREM cross-section images that for low twist angles ($\Psi \leq 5°$), interfacial screw dislocation segments are dissociated into two Shockley partials (**a/2[110]** → **a/6[211] + a/6[12$\bar{1}$]**), separated by an intrinsic stacking fault ribbon along (111) planes **[22]**. The segments dissociate outside the (001) interfacial plane ; **a/6[211]** along +z and **a/6[12$\bar{1}$]** along –z. The segments and their orientation can be presented in a ABCD scheme of a Thompson tetrahedron in [001] projection ***(Fig. 3a)*** or in 3D ***(Fig. 3c)*** **[23]**. The screw

dislocations belong to two families whose Burgers vectors are ***AB*** = **a/2[$\bar{1}$10]** and ***DC*** = **a/2[$\bar{1}\bar{1}$0]**. The Burgers vectors of the segments attached to the first family are ***Aδ*** = **a/6[12$\bar{1}$]** and ***δB*** = **a/6[$\bar{2}\bar{1}$1]** while those related to the second family ***Dβ*** = **a/6[$\bar{2}$1$\bar{1}$]** and ***βC*** = **a/6[1$\bar{2}$1]**.

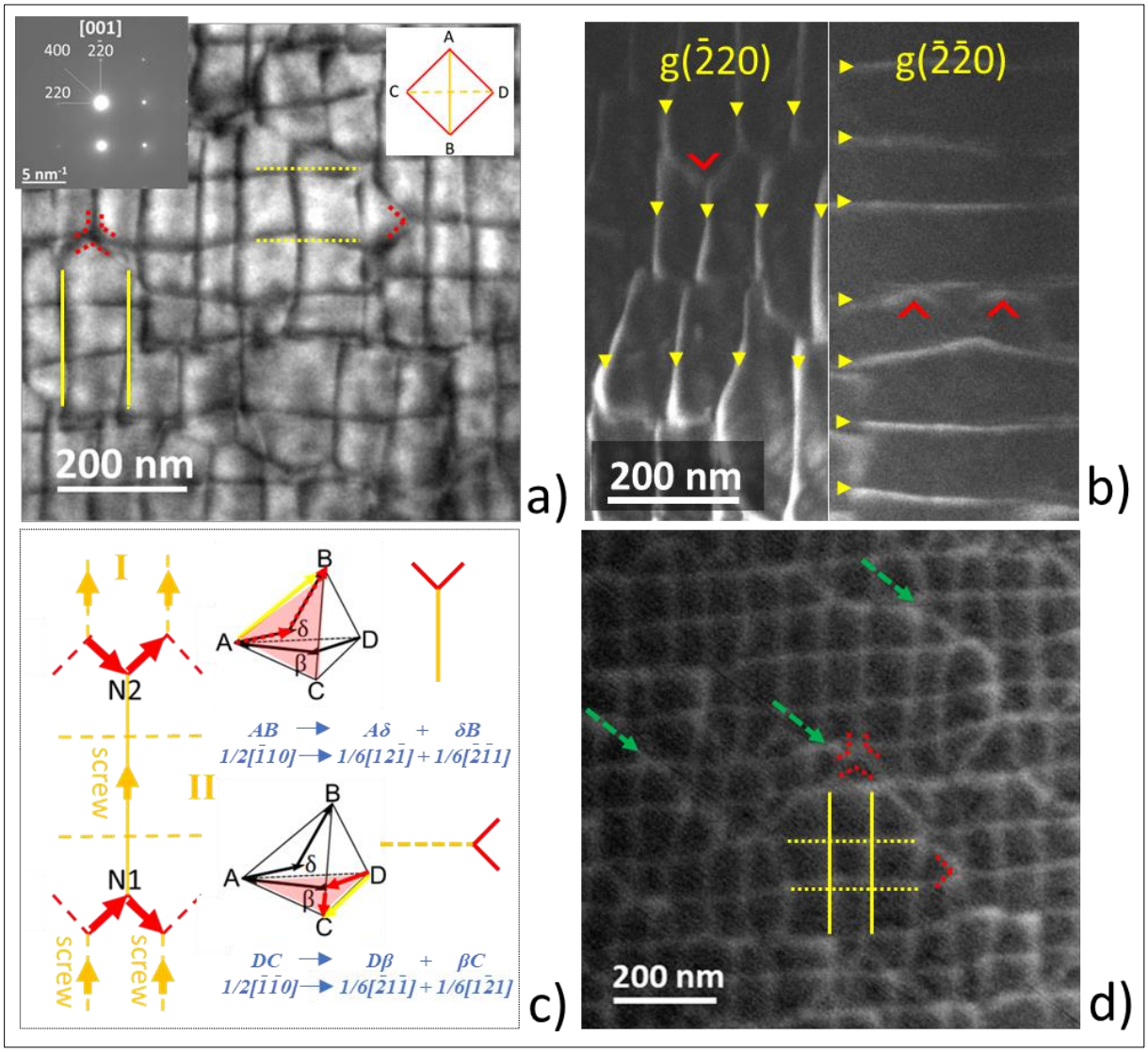

Figure 3: DN1 in plane view. (a) BF image in [001] zone axis and corresponding ED pattern in inset. The 3-fold segments (red) consist of one long segment (yellow) connected to two short segments (red) defined in a projected Thompson tetrahedron. The long segments form square patterns. (b) DF images using ***g*(**$\bar{2}$**2**0**)** (left) and ***g*(**$\bar{2}\bar{2}$**0)** (right) diffraction wave vectors, highlighting the nature of the screw segments (yellow arrows) and mixed partial segments (red arrows). (c) Schematic representation of the dislocation segments in the elongated hexagonal cells and in a 3D Thompson tetrahedron. (d) STEM-DF image showing that the curved lines made up of partial segments follow a main direction [100] (green arrows).

A DF-STEM image shows that the short dissociated segments follow curved lines whose main direction is [100] (green arrows) ***(Fig. 3d)***. These lines, called by Benamara et al., 60°-dislocation lines, compensate for the tilt component in a perpendicular direction **[24]**. The periodic spacing measured between the screw segments (long segments L) is $d_{L\text{-}DN1}$ = 82 (±11) nm while the one between the 60°-dislocation lines (composed of short segments S) is $d_{S\text{-}DN1}$ = 275 (±20) nm, corresponding respectively to a twist angle, $\Psi_{L\text{-}DN1}$ = 0.27 ± 0.1° ($b_{\Psi\text{-}DN1} = d_{110}$ = 0.384 nm), and a tilt angle, $\theta_{S\text{-}DN1}$ = 0.05 ± 0.1° ($b_{\theta\text{-}DN1}=d_{100}/2$ = 0.272 nm), according to the Frank's rule (Eq. 1). Both angle values are within the uncertainties of the wafer bonding process applied to our samples.

The observation of the cross-section lamella in [110] zone axis shows a Si/Si interface about 40 nm wide buried below the Si/oxide interface ***(Fig. 4a)***. The spatial layout is not distributed on a single plane due in particular to the dissociation of the short segments outside the [001] interface. Images recorded in [553] zone axis ***(Fig. 4b)***, which is inclined of about 20° with respect to [110] following a direction perpendicular to the interface, highlight features similar to those seen in plane-view (i.e. three-fold segments, long and short segments). In particular, it shows that the long segments are oriented parallel to the Si/oxide interface. Moreover, the capping formed by the short segments, which are attached to one family of screw segments, interacts and deflects the screw segments of the second family ***(Fig. 4b bottom)***.

From the HREM images in [110] zone axis ***(Fig. 4c)***, the gliding of the dissociated Shockley partials on {111} planes is highlighted. An enlarged image ***(Fig. 4d)*** of the defect located on the left side of the interface (yellow hatched line) shows the displacement of the atomic planes along the $[\bar{1}10]$ and $[\bar{1}12]$ directions on either side of the slip plane.

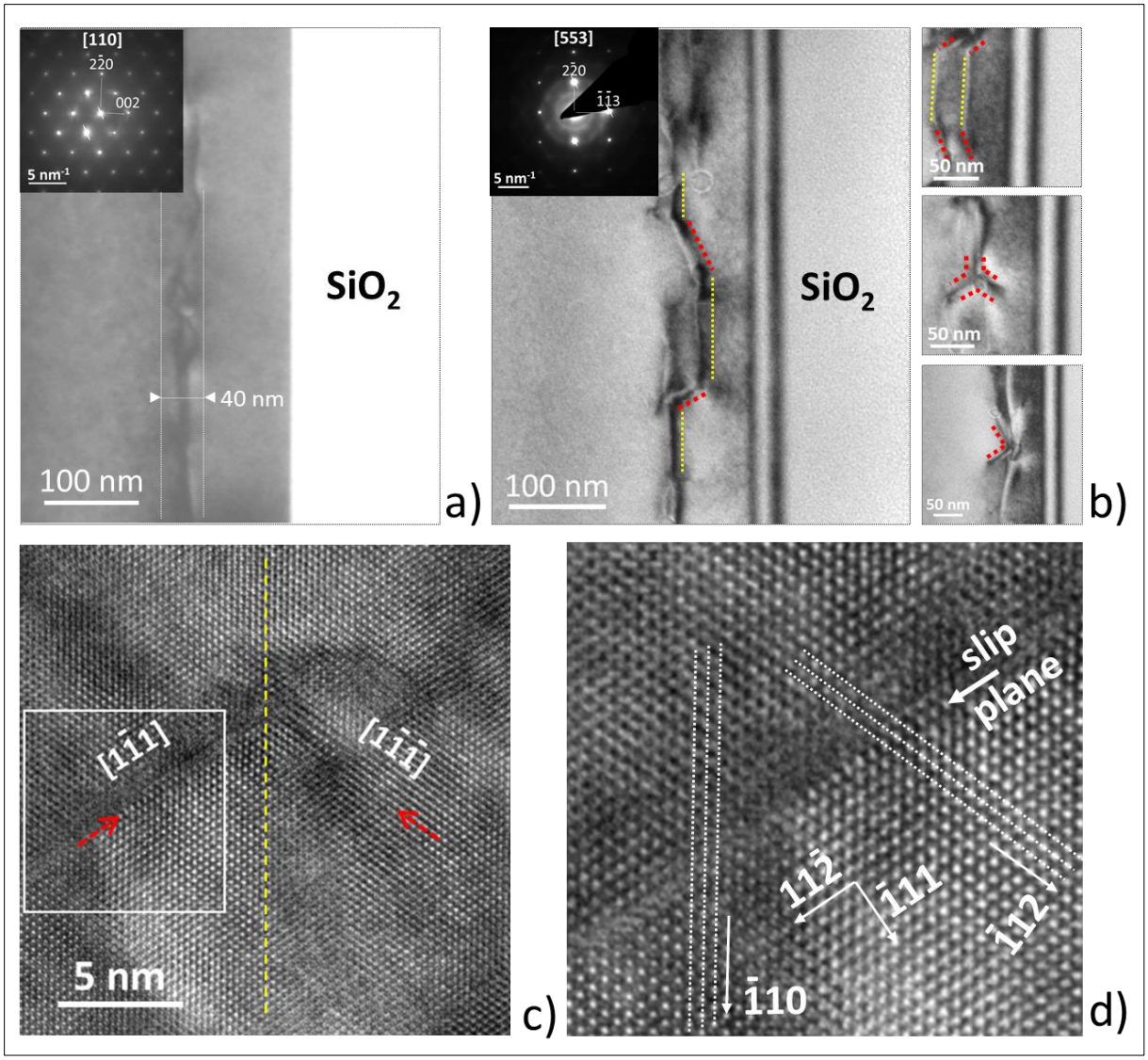

Figure 4: DN1 in cross section. a) BF image observed in [110] zone axis. b) BF image in [553] zone axis allowing a better visualization of the DN1 arrangement in cross-section (left). The right part of the figure shows long screw segments (yellow) and short partial segments (red) (top), as well as three-fold segments (middle) and partial segment caps (down). c) HREM image showing that the Shockley partials (pointed with red arrows) glide on {111} planes on both sides of the interface (yellow dotted line). d) Enlarged image of c) (inset) showing the displacement of the atomic planes along the [$\bar{1}$10] and [$\bar{1}$12] directions on either side of the slip plane.

3.2.DN2

Similar to DN1, a network exhibiting three-fold segments with extended hexagonal cells was also observed for DN2 ***(Fig. 5)***. However, fundamental differences concern the orientation and the nature of the dislocations. Indeed, the long segments of the hexagonal cells follow two

perpendicular directions <110> in the case of DN1, but one direction [100] only for DN2 ***(Fig. 5a)***. For the latter, an angle value of 4° (±1°) was measured between the direction of the long segments and [100]. 60°-dislocation lines formed by the partial segments were found to follow curved lines with a main direction [100] in DN1. This feature is different for DN2 since the short segments follow a more regular direction along [010]. Another notable characteristic of DN2 is the presence of broad dark fringes in the thick areas that follow the same direction [100] as the long segments and bend at the position of the short segments. A blue square pattern drawn on DN2 highlights a similar periodicity around 420 (±5) nm between the dark fringes and between the lines of the short segments. BF images recorded by tilting 20° relative to [001] in a direction along $[0\bar{1}0]$ show that the long and short segments arrange the dislocation network in a step-like pattern ***(Fig. 5b)***.

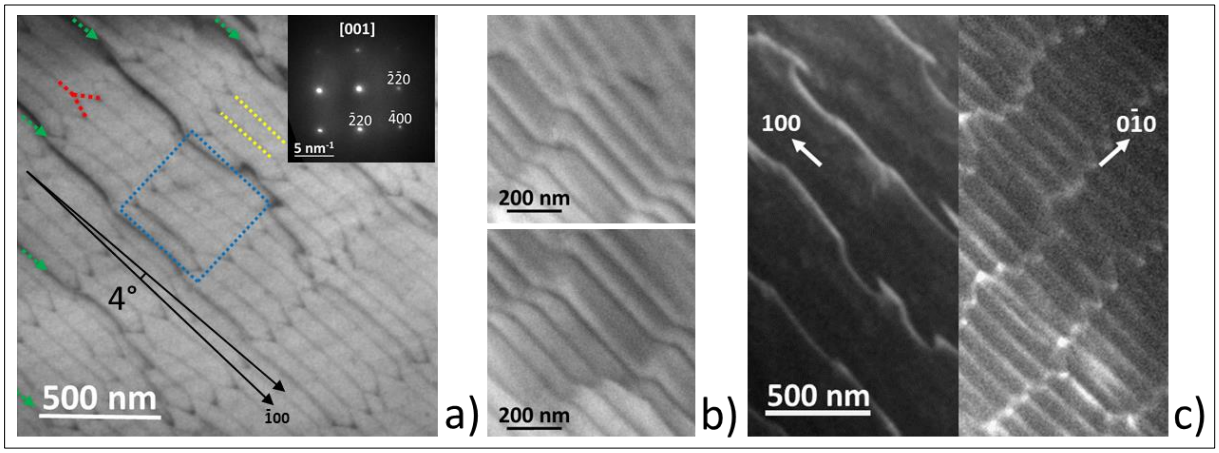

Figure 5: DN2 in plane view. (a) BF image in [001] zone axis showing the black fringes (green arrows), the three-fold segments (red) and the long segments (yellow). The ED pattern displayed in insert shows that the long segments are aligned along the [100] axis with a small deviation of 4°. The blue square highlights the similar periodicity between the black fringes and the lines of short segments. (b) BF images produced by tilting of 20° perpendicular to the long segments from the [001] zone axis. (c) DF images made using $\boldsymbol{g(400)}$ (left) and $\boldsymbol{g(040)}$ (right) diffraction wave vectors.

2-beam DF images show an inverted contrast between the long segments and the fringes both aligned along the same direction [100] ***(Fig. 5c)***. Indeed, the image produced from the diffraction wave vector $\boldsymbol{g(400)}$ highlights the fringes but not the long segments. Conversely,

the long segments are visible on images produced from a perpendicular wave vector ***g*(040)**, but not the fringes. According to these results, the fringes seem to exhibit at least a screw component of the Burgers Vector (***B***) along [100], while the long segments have an edge component perpendicular to [100]. Rouvière et al. explained that interfacial dislocations, with quite similar features than the black fringes aligned along the long segments, tend to be associated by pairs. Each one has a symmetrically related ***B*** with a ***a/2*** component along [001], introducing an interfacial step of height a/2 **[25]**.

Information concerning the short segments were obtained from DF contrast analyses in [101] zone axis. This orientation maintains the symmetry between two short segments leaving a node ***(Fig. 6a)***. In addition, the corresponding electron diffraction pattern contains other diffracted wave vectors to identify the dislocation type. Regarding the capping composed of two segments pointing along the direction [$\bar{2}02$], the left segment is invisible using ***g*(1$\bar{3}$1)** giving **a/6[$\bar{2}$11], a/6[1$\bar{1}\bar{2}$] and a/2[101]** as possible Burgers verctor ***(Fig. 6b)***. The segment is also invisible with ***g*(2$\bar{2}$2),** which excludes **a/6[$\bar{2}$11]** and **a/6[1$\bar{1}\bar{2}$],** but allows **a/2[101]**. The right segment is invisible with ***g*(3$\bar{3}$3)** giving the same ***B*** = **a/2[101]**. The short segments are thus characterized as 60°-mixed dislocations gliding along {111} planes, whose lines are directed along <110> directions with a Burgers vestor ***B*** = **a/2[101]**.

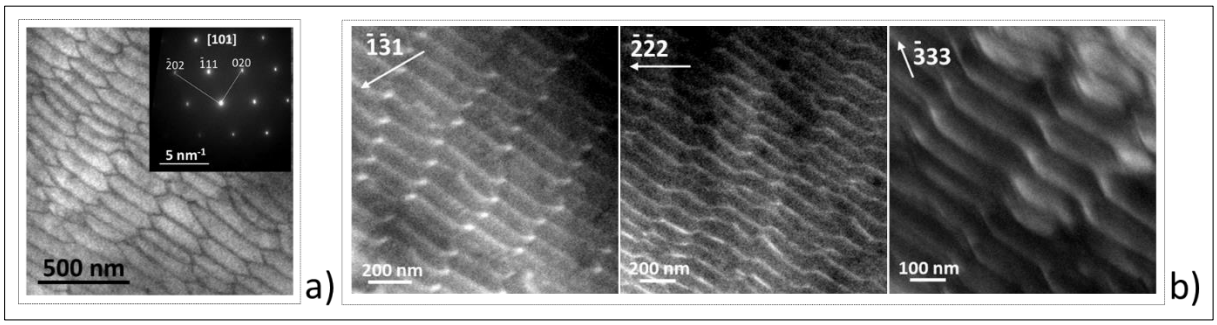

Figure 6 : (a) BF image and corresponding ED pattern (in insert) in [101] zone axis. (b) DF images in 2-beam condition using ***g*(1$\bar{3}$1)** (left), ***g*(2$\bar{2}$2)** (middle) and **g(3$\bar{3}$3)** diffraction vectors.

The observation of the lamella prepared in [110] cross-section shows a larger Si/Si interface (~ 60 nm) buried under the oxide layer, compared to DN1 ***(Fig. 7a)***. A BF-STEM image in [010] zone axis produced by tilting the lamella in a direction parallel to the interface from [110] ***(Fig. 7b)*** confirms the step arrangement formed by the long and short segments. In particular, contrary to DN1, the long segments are not parallel to the oxide interface.

The slight deviation of the long segments from [100] plus the results of DF contrast analyses rule out the screw and edge types for these dislocations, as explained hereafter. The contrast of the long segments are deactivated using a parallel diffracted wave vector ***g*(400)** from the plane view analysis ***(Fig. 5c left)***, which rules out the screw type. Also, from the DF images of the cross-section lamella ***(Fig. 7c down)***, the DN contrast is deactivated using ***g*(400)**, parallel to the layer surface. This result means the black fringes 420 (±5) nm apart are not contained in the lamella thickness, since the contrast would be activated, as it was observed in plane view. The DN contained in the cross-section lamella, which is therefore mainly composed of long segments, is activated using $\boldsymbol{g(00\bar{4})}$ ***(Fig. 7c up)***. These segments are therefore not **a[010]** edge dislocations **(*B* along *b*)** since the contrast would be deactivated. Also, **a[001]** edge dislocations (***B*** along ***c***) would present a deactivated contrast in plane view using ***g*(040)**, which is not the case ***(Fig. 5c right)***.

The data obtained on the DN2 sample show the presence of climbing long segments that are not exactly oriented along [100] and **a/2<101>** dislocations forming a 3D network arranged in steps. The climbing can be explained by the fact that the horizontal interface is not a glide plane for these interfacial dislocations **[26, 27].**

The average distance $d_{L\text{-}DN2}$ = 86 (±14) nm between the long segments is similar to $d_{L\text{-}DN1}$ = 82 (±11) nm while that between the lines of short zigzag segments $d_{S\text{-}DN2}$ = 420 (±5) nm is much larger and more regular than $d_{S\text{-}DN1}$ = 275 (±20) nm. The twist and tilt angles are

determined from the distances $d_{L\text{-}DN2}$ and $d_{S\text{-}DN2}$, respectively, using $b_{\Psi\text{-}DN2} = b_{\theta\text{-}DN2} = d_{100}/2$. The values are quite similar but nevertheless lower than those found for DN1 ($\Psi_{L\text{-}DN2} = 0.18° < \Psi_{L\text{-}DN1} = 0.27°$ and $\theta_{S\text{-}DN2} = 0.03° < \theta_{S\text{-}DN1} = 0.05°$). These results also highlight the important fluctuation of the distances ($d_{S\text{-}DN2.} = 420$ (±5) nm >> $d_{S\text{-}DN1} = 275$ (±20) nm) for misorientation angles close to 0° ($\theta_{S\text{-}DN1} = 0.05°$ and $\theta_{S\text{-}DN2} = 0.03°$), which is a direct consequence of the Frank's rule (Eq. 1).

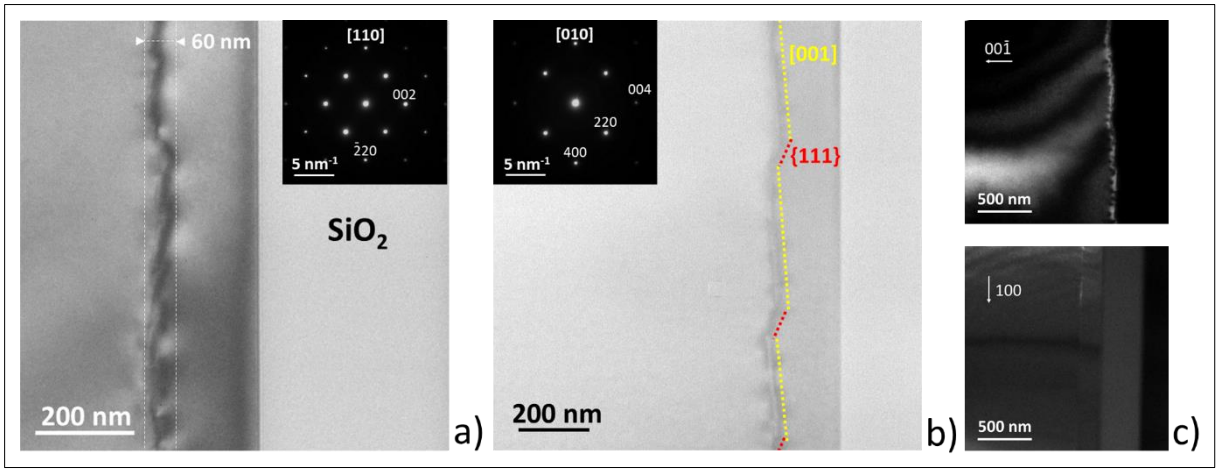

Figure 7: DN2 in cross section. (a) BF image observed in [110] zone axis. (b) BF-STEM image of the cross-section lamella in [010] zone axis highlighting the 3D arrangement of the long (yellow) and short (red) segments. (c) DF images using $\boldsymbol{g(00\bar{4})}$ and ***g*(400)** diffraction wave vectors.

4. Discussion

Diagrams of the DN1 ($\Psi_{L\text{-}DN1} = 0.27°$; $\theta_{S\text{-}DN1} = 0.05°$) and DN2 ($\Psi_{L\text{-}DN2} = 0.18°$; $\theta_{S\text{-}DN2} = 0.03°$) networks are presented in Figure 8. In each case, the DNs can be schematized by modules of hexagonal cells. In DN1, the cells are randomly ordered along two perpendicular <110> directions (orange arrows) of the [001] interface in such a way that the dissociated Shockley dislocations follow a [100] direction (blue arrows) ***(Fig. 8a)***. In DN2, the cells are more regularly ordered side by side in groups of 3 members along the [010] direction, which are separated by interfacial steps ***(Fig. 8b)***. No threading dislocation, that extends from the surface through the strained layer, was observed in both samples.

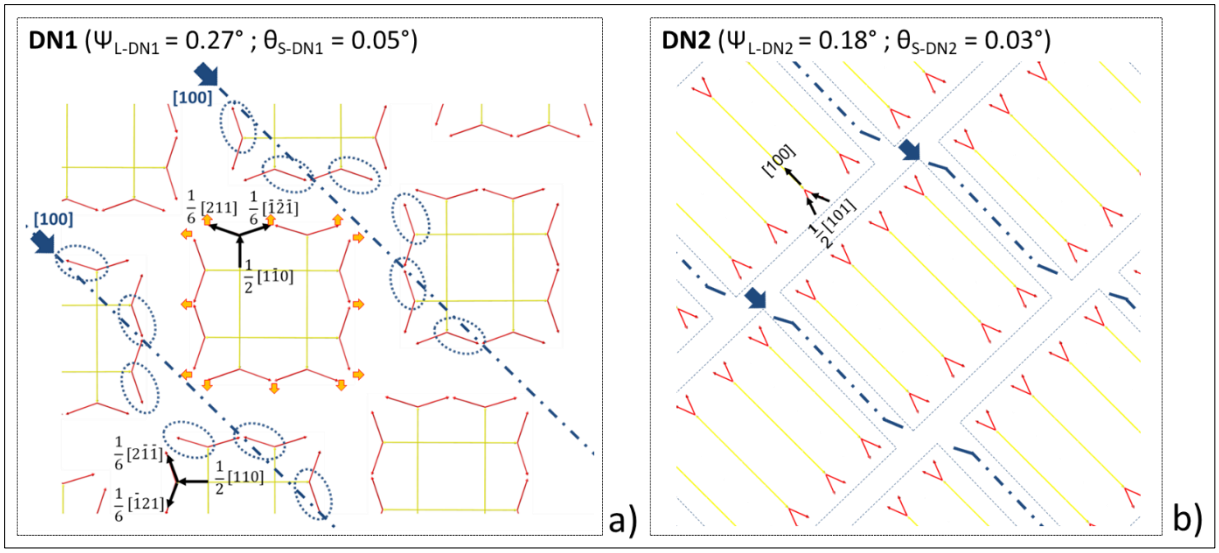

Figure 8 : Diagrams of the DN1 and DN2 networks. (a) DN1 : Hexagonal cells are formed by long **a/2<110>** screw dislocation segments which dissociate in two shorter Shockley partials. The Shockley partials follow a curved direction along [100]. (b) DN2 : Hexagonal cells consist of climbing long segments deviated of 4° from [100], as well as shorter **a/2[101]** segments. The hexagonal cells are ordered by 3 members in large square patterns separated by interface steps directed along [100] that curved around the short segments.

Theoretical and experimental studies have shown that the minimum energy configuration of the DNs in FCC {100} interfaces is the square shape consisting of two orthogonal sets of parallel screw dislocation lines **a/2<110>** forming four-fold nodes at the intersections **[28, 29]**. This geometry was obtained by Fournel et al., thanks to a WB made with a very low tilt angle of less than 0.01° **[19]**. It is generally accepted that the Burgers vectors **a/2<110>** of screw dislocations are favored, since they correspond to the smallest interatomic spacing in the {100} planes and therefore to the smallest dislocation line energy. Mechanisms of interaction between initial dislocations to form the low-energy configuration of three-fold nodes have been proposed **[21]**. The twist accommodation requires two equal resulting screw components along two orthogonal directions ; that is why, in most cases, it is accommodated by a 2D square network of screw dislocations. The tilt accommodation requires an edge component of the resulting ***B*** normal to the GB, giving mixed partial dislocations that point out of the interface plane. The dissociation operation into partial dislocations reduces the total

energy of the interface **[30, 31]**. The DN stabilization represents a balance between the driving and opposing forces, due to the repulsion between the parallel segments **[28]**.

Akatsu et al., have analyzed the influence of the twist and tilt angles on the DN geometries **[32]**. For (Ψ = 2.53°, θ = 0.56°), the DN presented two sets of **a/2<110>** screw dislocations composed of horizontal segments and vertical lines forming square patterns of about 8 nm side. Additionally, zigzag tilt segments, spaced approximately 25 nm apart, were mainly located along the same vertical direction <110> forming 3-fold nodes with the horizontal screw segments. For a two to five times smaller range of twist angles (Ψ = 1.34 - 0.5°) and a somewhat smaller range of tilt angles (θ = 0.53 - 0.49°), vertical fringes were clearly visible with spacings from 25 nm to 170 nm. Additionally, horizontal screw segments and vertical lines of zigzag segments tended to form hexagonal cells with sides of approximately 25 nm. Finally, for the smallest misorientation angles (Ψ = 0.539°, θ = 0.083°), a network similar to DN1 was obtained with vertical and horizontal segments forming smaller square patterns with sides of about 40 nm. Fringes of tilt dislocations, spaced of about 200 nm and deviated by 25° from the vertical <110> direction, crossed the screw dislocations to form three-fold nodes. Fournel et al., have also observed a DN with similar geometric characteristics but with smaller square patterns using higher misorientation angles (Ψ = 2.75°, θ = 0.34°) **[19]**. The DN consisted of square patterns with sides of approximately 8 nm as well as fringes of tilt dislocations, spaced 40 nm apart, which were deviated by approximately 28° from the vertical screw dislocations.

DN1 (Ψ = 0.27°, θ = 0.05°) is composed of lines of tilt dislocations spaced 275 (±20) nm apart mainly oriented along **[100]**, therefore deviated by 45° from the vertical screw segments **a/2<110>**. In summary, as the twist and tilt angles tend toward 0°, in addition to the increasing spacing between the tilt dislocations composed of fringes and lines of short zigzag segments, the deviation of the tilt fringes tends to the **[100]** axis.

Concerning the WB prepared using an additional rotation of 90°, Vdovin et al., observed an interfacial DN exhibiting similar characteristics to DN2 **[21]**. In particular, the resulting network also made it difficult to analyze the dislocation types since the behaviour contrasts did not match to conventions usually found for fcc structures. The distance between the fringes and between the lines of zigzag dislocations was around 200 nm, about half that found for DN2, therefore obtained using a higher tilt angle. The distance between the long segments was quite similar to that of DN2 resulting from an assumed similar twist angle. The network analyzed by Vdovin et al., was more distorted and irregular. Furthermore the long segments and tilt fringes, both parallels, were deviated by 32° relative to a direction <110>, or by 13° relative to <100>. Thus, for WBs obtained with an additional rotation of 90°, the DNs appear more regular with less distorsion when the twist and tilt angles are close to 0°, as it is the case with DN2. In addition, the orientations of the long segments of the elongated hexagonal cells as well as the tilt fringes are closer to [100] directions.

The distance between the long **a/2<110>** screw segments in DN1 ($d_{L\text{-}DN1}$ = 82 (±11) nm) is quite similar to that between the long segments slightly deviated from [100] in DN2 ($d_{L\text{-}DN2}$ = 86 (±14) nm). However, the distance between the lines of short segments is much longer in DN2 ($d_{S\text{-}DN2.}$ = 420 (±5) nm) than in DN1 ($d_{S\text{-}DN1}$ = 275 (±20) nm). This results in longer segments in DN2 than in DN1. The DN2 structure should therefore require a higher total dislocation energy than DN1. The assumed lower free energy of the DN1 interface is neither related to the heating temperature nor to the misorientation angles from <110> directions since the corresponding values are quite similar to those used for DN2. The difference in free energy and therefore the net change of geometry in each DN is mainly due to the additional rotation of 90° between the initial wafers before bonding. Indeed, the origin of the tilt dislocations are attributed to the surface miscut steps formed during the wafer cutting process. The initial step structures of both wafers are incorporated as a set of tilt dislocations by diffusion at the interface

with regular spacing during the heat treatments **[32]**. This can be understood from the figure 1c which shows how the rotation between the two wafers modifies the geometry formed by the surface steps where the short segments take place. A wafer bonding processed without additional rotation of 90° promotes the formation of DN1, in which two sets of hexagonal cells arrange in the diagonals of the square patterns formed by the surface steps oriented along two <100> directions. A wafer bonding processed with an additional rotation of 90° promotes the formation of DN2, in which one set of hexagonal cells arranges side by side in strips formed by the surface steps oriented along one direction <100>. The dissociation of the two sets of **a/2<110>** screw segments into Shokley partials takes place on the two perpendicular sets of interfacial steps in DN1. For DN2, the question about the formation mechanisms remains opened. In one hand, the long segments can dissociate in two **a/2<101>** short segments. In another hand, the long segments could have been formed after the combination of two dissimilar primary dislocations **a/2<101>** between two operative octahedral glide systems (111) and $(1\bar{1}\bar{1})$. In the latter case, this kind of mechanism is suggested in the case of **a<100>** edge dislocations in (001) interfaces of nickel-based single-crystal fcc superalloys prepared at high-temperature and low-stress creep **[33, 34]**. By analogy, the **a/2<101>** dislocations in DN2 could have been introduced at the early stage of the wafer bonding and have received the highest elastic force coming from the action of the misfit stress generated by the angular mismatch at interfaces.

Conclusion

Two models of interfacial dislocation networks, made by wafer bonding process using misorientation angles close to 0° relative to <110> axes, were analyzed. Among them, one model was prepared by adding a rotation of 90° on an initial wafer in the pair, changing significantly the character, the morphology and the core structure of the dislocations. For the DN obtained at higher misorientation angle (DN1 - $\Psi_{L\text{-}DN1} = 0.27°$; $\theta_{S\text{-}DN1} = 0.05°$) without any additional 90°-rotation of a wafer in the pair, in-plane interfacial screw segments **a/2<110>** dissociate into two out-of-plane interfacial Shockley partial segments. At lower misorientation angles with an additional 90°-rotation of a wafer in the pair (DN2 - $\Psi_{L\text{-}DN2} = 0.18°$; $\theta_{S\text{-}DN2} = 0.03°$), climbing segments slightly deviated from the [100] axis and out-of-plane interfacial segments **a/2<101>** were found. In each case, fringes of tilt dislocations are mainly oriented along **<100>** axes due to the position of the interfacial steps originating from the miscuts present in the initial wafers before bonding.

Future research focusing on the analysis of samples prepared with a 90°-rotation at even smaller misorientation angles, close to 0° with respect to an axis <110> could shed light on the formation mechanisms and the possibility of producing new DNs with real edge dislocation segments as well as other dislocation types, in or out of the interface plane.

References

[1] Wang, P., Cui, C., Yang, D., & Yu, X. (2020). Seed-assisted growth of cast-mono silicon for photovoltaic application: challenges and strategies. Solar Rrl, 4(5), 1900486.

[2] Reiche, M., Kittler, M., Erfurth, W., Pippel, E., Sklarek, K., Blumtritt, H., Haehnel, A. & Uebensee, H. (2014). On the electronic properties of a single dislocation. Journal of Applied Physics, 115(19).

[3] Laconte, J., Akheyar, A., Raskin, J.-P. & Flandre, D. MicroElectroMechanical Systems in Silicon-on-Insolator Technology.

https://dial.uclouvain.be/pr/boreal/object/boreal%3A240317/datastream/PDF_01/view

[4] Benamara, M., Rocher, A., Sopéna, P., Claverie, A., Laporte, A., Sarrabayrouse, G., Lescouzères, L. & Peyre-Lavigne, A. (1996). Structural and electrical investigations of silicon wafer bonding interfaces. Materials Science and Engineering: B, 42(1-3), 164-167.

[5] Ljungberg, K., Grey, F., & Bengtsson, S. (1997). Formation of directly bonded Si/Si interfaces in ultra-high vacuum. Applied surface science, 117, 813-819.

[6] Fedotov, A., Saad, A. M., Enisherlova, K., & Mazanik, A. (2002). Electrical characterization of interfaces in unitype directly bonded silicon wafers. Materials Science and Engineering: B, 91, 384-388.

[7] Fournel, F., Moriceau, H., Magnea, N., Eymery, J., Rouvière, J. L., Rousseau, K., & Aspar, B. (2000). Ultra thin silicon films directly bonded onto silicon wafers. Materials Science and Engineering: B, 73(1-3), 42-46.

[8] Wind, R. A., Murtagh, M. J., Mei, F., Wang, Y., Hines, M. A., & Sass, S. L. (2001). Fabrication of nanoperiodic surface structures by controlled etching of dislocations in bicrystals. Applied Physics Letters, 78(15), 2205-2207.

[9] Ieong, M., Doris, B., Kedzierski, J., Rim, K., & Yang, M. (2004). Silicon device scaling to the sub-10-nm regime. Science, 306(5704), 2057-2060.

[10] Ejeckam, F. E., Seaford, M. L., Lo, Y. H., Hou, H. A., & Hammons, B. E. (1997). Dislocation-free InSb grown on GaAs compliant universal substrates. Applied physics letters, 71(6), 776-778.

[11] Coelho, J., Patriarche, G., Glas, F., Sagnes, I., & Saint-Girons, G. (2005). Dislocation networks adapted to order the growth of III-V semiconductor nanostructures. physica status solidi (c), 2(6), 1933-1937.

[12] Maleville, C., & Mazuré, C. (2004). Smart-Cut® technology: from 300 mm ultrathin SOI production to advanced engineered substrates. Solid-State Electronics, 48(6), 1055-1063.

[13] Di Cioccio, L., Jalaguier, E., & Letertre, F. (2004). Compound Semiconductor Heterostructures by Smart Cut™: SiC On Insulator, QUASIC™ Substrates, InP and GaAs Heterostructures on Silicon. In Wafer Bonding: Applications and Technology (pp. 263-314). Berlin, Heidelberg: Springer Berlin Heidelberg.

[14] Cahn, J. W., Mishin, Y., & Suzuki, A. (2006). Coupling grain boundary motion to shear deformation. Acta materialia, 54(19), 4953-4975.

[15] Patout, L., Hallaoui, A., Neisius, T., Campos, A. P., Dominici, C., Alfonso, C., & Charaï, A. (2018). Origin of the superstructure elucidated by atomic resolution HAADF-STEM and HREM in the Ce10W22O81 lanthanide tungstate phase. Journal of Applied Crystallography, 51(2), 344-350.

[16] Patout, L., Alfonso, C., & Charaï, A. (2020). Ordered vacancies in the fluorite and perovskite layers of the lanthanide BiLuWO6 phase by HREM. Materialia, 9, 100545.

[17] Schaffer, B. (2016). Digital micrograph. Transmission Electron Microscopy: Diffraction, Imaging, and Spectrometry, 167-196.

[18] Yin, Y. W. (2004). CrystalMaker 6.3 CrystalMaker Software, Begbroke Science Park, Building 5, Sandy Lane, Yarnton OX5 1P5, UK http://www. crystalmaker. com. 599.00(singleuser), 415.00 (academic, single user). Contact company for other pricing options.

[19] Fournel, F., Moriceau, H., Aspar, B., Rousseau, K., Eymery, J., Rouviere, J. L., & Magnea, N. (2002). Accurate control of the misorientation angles in direct wafer bonding. Applied physics letters, 80(5), 793-795.

[20] Boussaid, A., Fnaiech, M., Fournel, F., & Bonnet, R. (2005). Zigzag lines in a (001) Si low-angle twist boundary. Philosophical Magazine, 85(11), 1111-1122.

[21] Vdovin, V., Vyvenko, O., Ubyivovk, E., & Kononchuk, O. (2011). Mechanisms of dislocation network formation in Si (001) hydrophilic bonded wafers. Solid State Phenomena, 178, 253-258.

[22] Rousseau, K., Rouvière, J. L., Fournel, F., & Moriceau, H. (2001). Structural characterization of ultra-thin (0 0 1) silicon films bonded onto (0 0 1) silicon wafers:: a transmission electron microscopy study. Materials Science in Semiconductor Processing, 4(1-3), 101-104.

[23] Amelinckx, S. (1956). The direct observation of dislocation nets in rock salt single crystals. Philosophical Magazine, 1(3), 269-290.

[24] Benamara, M., Rocher, A., Sopéna, P., Claverie, A., Laporte, A., Sarrabayrouse, G., Lescouzères, L. & Peyre-Lavigne, A. (1996). Structural and electrical investigations of silicon wafer bonding interfaces. Materials Science and Engineering: B, 42(1-3), 164-167.

[25] Rouviere, J. L., Rousseau, K., Fournel, F., & Moriceau, H. (2000). Huge differences between low-and high-angle twist grain boundaries: The case of ultrathin (001) Si films bonded to (001) Si wafers. Applied Physics Letters, 77(8), 1135-1137.

[26] Huang, M., Cheng, Z., Xiong, J., Li, J., Hu, J., Liu, Z., & Zhu, J. (2014). Coupling between Re segregation and γ/γ′ interfacial dislocations during high-temperature, low-stress creep of a nickel-based single-crystal superalloy. Acta materialia, 76, 294-305.

[27] Sarosi, P. M., Srinivasan, R., Eggeler, G. F., Nathal, M. V., & Mills, M. J. (2007). Observations of a<010> dislocations during the high-temperature creep of Ni-based superalloy single crystals deformed along the [001] orientation. Acta materialia, 55(7), 2509-2518.

[28] Hirth, J. P., & Feng, X. (1990). Critical layer thickness for misfit dislocation stability in multilayer structures. Journal of applied physics, 67(7), 3343-3349.

[29] Tang, E., & Fu, L. (2014). Strain-induced partially flat band, helical snake states and interface superconductivity in topological crystalline insulators. Nature Physics, 10(12), 964-969.

[30] Shao, S., Wang, J., & Misra, A. (2014). Energy minimization mechanisms of semi-coherent interfaces. Journal of Applied Physics, 116(2).

[31] Dai, S., Xiang, Y., & Srolovitz, D. J. (2014). Atomistic, generalized Peierls–Nabarro and analytical models for (1 1 1) twist boundaries in Al, Cu and Ni for all twist angles. Acta materialia, 69, 162-174.

[32] Akatsu, T., Scholz, R., & Gösele, U. (2004). Dislocation structure in low-angle interfaces between bonded Si (001) wafers. Journal of materials science, 39, 3031-3039.

[33] Sarosi, P. M., Srinivasan, R., Eggeler, G. F., Nathal, M. V., & Mills, M. J. (2007). Observations of a<010> dislocations during the high-temperature creep of Ni-based superalloy single crystals deformed along the [001] orientation. Acta materialia, 55(7), 2509-2518.

[34] Lv, X., & Zhang, J. (2017). Core structure of a<100> interfacial superdislocations in a nickel-base superalloy during high-temperature and low-stress creep. Materials Science and Engineering: A, 683, 9-14.